PAPER

Check for updates

Electrostatic control of photoluminescence from A and B excitons in monolayer molybdenum disulfide†

Yuchun Liu, [ID] Tianci Shen, Shuangyi Linghu, [ID] Ruilin Zhu and Fuxing Gu [ID] *

Tailoring excitonic photoluminescence (PL) in molybdenum disulfide (MoS_2) is critical for its various applications. Although significant efforts have been devoted to enhancing the PL intensity of monolayer MoS_2, simultaneous tailoring of emission from both A excitons and B excitons remains largely unexplored. Here, we demonstrate that both A-excitonic and B-excitonic PL of chemical vapor deposition (CVD)-grown monolayer MoS_2 can be tuned by electrostatic doping in air. Our results indicate that the B-excitonic PL changed in the opposite direction compared to A-excitonic PL when a gate voltage (V_g) was applied, both in S-rich and Mo-rich monolayer MoS_2. Through the combination of gas adsorption and electrostatic doping, a 12-fold enhancement of the PL intensity for A excitons in Mo-rich monolayer MoS_2 was achieved at $V_g = -40$ V, and a 26-fold enhancement for the ratio of B/A excitonic PL was observed at $V_g = +40$ V. Our results demonstrate not only the control of the conversion between A^0 and A^-, but also the modulation of intravalley and intervalley conversion between A excitons and B excitons. With electrostatic electron doping, the population of B excitons can be promoted due to the enhanced intravalley and intervalley transition process through electron–phonon coupling. The electrostatic control of excitonic PL has potential applications in exciton physics and valleytronics involving the B excitons.

Introduction

Two-dimensional (2D) transition metal dichalcogenides (TMDCs), especially molybdenum disulfide (MoS_2), have drawn worldwide attention due to their unique optical and electronic properties.[1–3] In particular, monolayer MoS_2 presents strong photoluminescence (PL) and large exciton binding energy, providing a new platform to realize the emerging developments in various ultrathin optoelectronic devices.[1,4–8] Due to the extremely large Coulomb interactions in atomically thin MoS_2, stable excitons can be generated from the electron–hole pairs induced by photoexcitation even at room temperature. Generally, PL in monolayer MoS_2 is dominated by the recombination of electrons in the conduction band with holes in the spin–orbit split valence bands, which refers to the A excitons and B excitons at the direct bandgap transition at the K and K' points. The energy of B-excitonic PL peaks is 100–200 meV higher than that of A excitons, corresponding to the valence band splitting due to the strong spin orbital.[9,10] Various intrinsic defects widely exist in MoS_2, which act as active centers for trapping molecules and chemical reactions. These defects greatly impact the carrier

concentration, exciton dynamics, and bandgap structure. Controlling the defects and carrier density is an effective method for modulating the PL properties of monolayer MoS_2.[11,12] Enhanced PL emission is generally achieved by promoting defect-related doping and trion-exciton transitions. The most widely reported strategies include depleting excessive electrons through gas physisorption,[13–15] chemical doping,[16,17] and direct carrier injection through electrical doping.[18,19] The O_2, H_2O and N_2 molecules can be directly adsorbed on chalcogen vacancies and electrons extracted from MoS_2.[13,14] The previous work involving chemical doping with bis(trifluoromethane) sulfonimide (TFSI), poly(4-styrenesulfonate) (PSS) and 7,7,8,8-tetracyanoquinodimethane (TCNQ) drastically enhanced the PL intensity of monolayer MoS_2. The electrically doped MoS_2 monolayers encapsulated in poly(methyl methacrylate) achieved a marked PL enhancement and near-unity quantum yields due to the mechanism of electron counter-doping without chemical defect passivation.[1] Indeed, extensive studies on the PL properties and exciton dynamics in MoS_2 have been reported, which focus on the interplay between neutral A excitons (A^0) and many-body bound states such as charged trions (A^-).[20–22] However, these studies are limited to the enhancement of A-excitonic PL emission and valley polarization.

The B-exciton emission of monolayer MoS_2 has only been investigated in a few studies.[23–26] It has been reported that PL

School of Optical-Electrical and Computer Engineering, University of Shanghai for Science and Technology, China. E-mail: gufuxing@usst.edu.cn

emissions from both A and B excitons can vary widely from sample to sample, which is related to the difference in non-radiative recombination associated with defect density in a given sample. B excitons exhibit a monotonic decline as the defect density increases in the monolayer MoS_2 prepared by the chemical vapor deposition (CVD) method.[24] Mikkelsen et al. demonstrated tunable emission wavelengths of the A and B excitons in monolayer MoS_2 by tuning the plasmonic nanocavity resonance; this method successfully achieved a dominant B-excitonic emission by overlapping the plasmon resonance with the B exciton energy.[25,26] McCreary et al. provided a facile method to assess sample quality: a low B/A ratio indicates a low defect density and high sample quality, while a large B/A ratio represents a high defect density and poor-quality material.[27] Sarkar et al. obtained a six-fold enhancement of the intrinsically weak B excitonic emission in few layers of MoS_2 : Ag nano-heterojunctions embedded into a glass matrix, which can be attributed to the dipole–dipole interactions via exciton–plasmon coupling at room temperature.[28] The simultaneous tailoring of emission form both A excitons and B excitons remains largely unexplored.

In this study, we explored the tunable excitonic PL from both A excitons and B excitons in monolayer MoS_2 on SiO_2/Si substrates prepared by the traditional CVD method. Electrostatic doping was performed through back-gate voltage (V_g) variation in a capacitor structure, demonstrating an effective control method for both A-excitonic and B-excitonic PL in monolayer MoS_2 in air at room temperature. Electrostatic doping allowed us to tune the B-excitonic PL intensity in a direction opposite to the A-excitonic PL. Electron injection induced by a positive V_g obviously enhanced the PL intensity from B excitons, while the A-excitonic PL was suppressed in both S-rich and Mo-rich monolayer MoS_2. Our results not only demonstrate good control of conversion between A^0 and A^- through a combination of gas adsorption and electrostatic doping, but also show the presence of intravalley and intervalley transitions between A excitons and B excitons. The B excitons would relax to A excitons when a negative V_g was applied, leading to reduced B-excitonic PL and increased A-excitonic PL. When the applied V_g became positive, the B exciton population was increased due to the enhanced intravalley and intervalley transitions from A excitons. These transitions can be mediated by flexural phonons in the realm of the Elliott–Yafet spin-flip mechanism through intrinsic electron–phonon scattering. Experimental results show that excitonic PL from both A and B excitons was effectively controlled by the electrostatic method. This could pave an additional pathway for investigating exciton physics and valleytronics in 2D TMDCs at room temperature.

Experimental section

Monolayer MoS_2 was prepared on SiO_2/Si substrates (280–300 nm SiO_2) by the CVD method in a double-zone furnace. Sulfur powder and molybdenum(VI) oxide (MoO_3) powder were used as precursors, with sulfur placed upstream and MoO_3 placed downstream of the two-zone furnace, respectively (as shown in Fig. S1 of the ESI†). The temperature of the central zone-I and zone-II were set to 300 °C and 850–870 °C for the sulfur and molybdenum precursor, respectively. High-purity argon gas (Ar) was introduced into a quartz tube with a flow rate of 100–150 sccm during the growth process. The growth time was about 10–20 minutes for monolayer MoS_2 in our growth system at nearly atmospheric pressure. The monolayer MoS_2 flakes with different qualities can be achieved by changing the Mo : S ratio of the precursor and the gas flow rate.[29–32] For the growth of S-rich monolayer MoS_2, 200 mg sulfur powder and 5 mg MoO_3 powder were used as precursors with an Ar flow rate of 100–120 sccm. For the growth of Mo-rich monolayer MoS_2, 200 mg sulfur powder and 10 mg MoO_3 powder were used as precursors with an Ar flow rate of 150 sccm.

Optical microscopy, atomic force microscopy (AFM), and Raman spectroscopy were used to characterize the CVD-grown monolayer MoS_2. Then a Au electrode was fabricated by sputtering with polydimethylsiloxanes (PDMS) masks at the micron scale. Electrostatic doping was conducted based on MoS_2 samples in a structure similar to a field-effect transistor (FET), with Au as the top electrode and Si as the back-gate electrode. PL spectra were collected using an IsoPlane spectrometer equipped with an emICCD (Princeton Instruments, PI-MAX4) under 532 nm continuous wave (CW) laser excitation. The Raman measurements were taken by using a Renishaw inVia Raman microscope under 532 nm laser excitation. The laser power intensity was $\sim10^3$ W cm^{-2} for PL and Raman spectra measurements with a spot size of ~2 μm. The electrostatic doping in the MoS_2 monolayer was systematically varied by using a DC voltage supplier. The MoS_2 samples exhibited electrostatic doping over the range of the gate voltage (-40 V to $+40$ V). All measurements were performed at room temperature under ambient air conditions.

Results and discussion

Fig. 1(a) shows the microscopy image of monolayer MoS_2 prepared by the CVD method. The thickness of triangular CVD-grown MoS_2 was ~0.85 nm, which is consistent with the monolayer thickness. The size of triangular monolayer MoS_2 was 30–70 μm. The absorption spectra and Raman spectra of the MoS_2 grown on SiO_2/Si substrates under relatively S-rich and Mo-rich conditions are shown in Fig. 1(b–c). Two distinguishing absorption peaks were observed in both S-rich and Mo-rich monolayer MoS_2, which relate to the A and B excitons. The Raman spectra peaks were located at ~384 cm^{-1} and ~404.5 cm^{-1} corresponding to the E^1_{2g} and A_{1g} peaks for the in-plane and out-of-plane vibration modes, respectively. The frequency differences (Δ) between E^1_{2g} and A_{1g} peaks were 20.6 cm^{-1} and 20.3 cm^{-1} for the S-rich and Mo-rich MoS_2, respectively, in accordance with the observed separation in the CVD-grown monolayer MoS_2 on SiO_2/Si.[33] It has been reported that n-type doping leads to a redshift of the A_{1g} peak and an increased line width of A_{1g}, whereas the E^1_{2g} peak is insensitive to the doping effect.[34,35] The Mo-rich MoS_2 sample showed a redshifted A_{1g} peak at 404.2 cm^{-1}, compared to that of the S-rich MoS_2 sample at 404.7 cm^{-1}. The Raman mode peaks of MoS_2
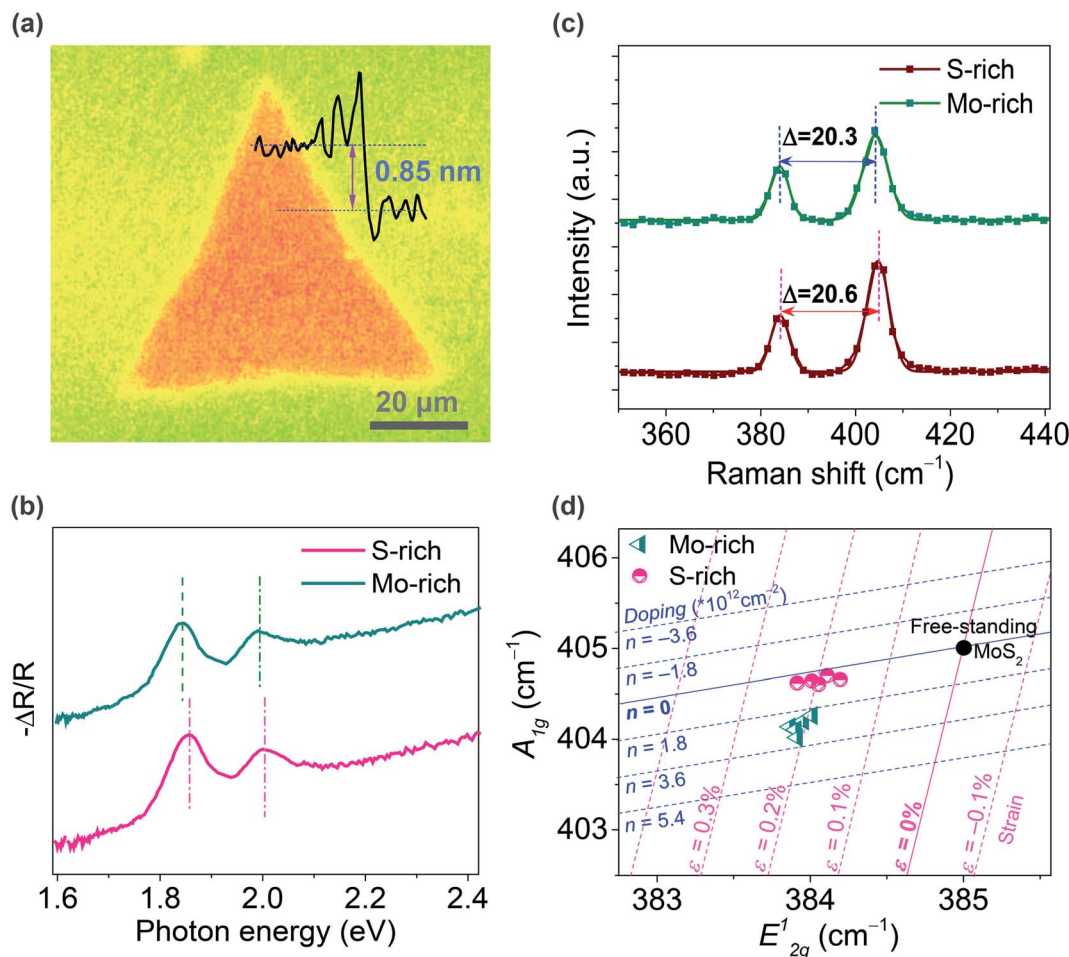
Fig. 1 (a) Microscopy image of the CVD-grown MoS_2 on a SiO_2/Si substrate; (b–d) Absorption spectra, Raman spectra, and the correlation plot (A_{1g} versus E^1_{2g}) of the S-rich and Mo-rich monolayer MoS_2.

grown on SiO_2/Si substrates were plotted on the Raman-derived doping-strain map, as shown in Fig. 1(d). The zero strain and zero doping lines crossed at a point, corresponding to the literature values ($E^1_{2g} = 385.0.2$ cm^{-1} and $A_{1g} = 405.0$ cm^{-1}) of the peak frequencies for a suspended MoS_2 membrane.[36–38] The correlation plot of the A_{1g} peak positions versus the E^1_{2g} peak positions suggest that the Mo-rich MoS_2 grown on SiO_2 shows a higher electron doping (2–3×10^{12} cm^{-2}) than that of the S-rich MoS_2 (0.5–1×10^{12} cm^{-2}). Raman peaks of both Mo-rich and S-rich MoS_2 were located near a strain line at $\varepsilon = 0.2\%$, indicting no obvious difference in the strain effect. Therefore, the peak shifts between the Mo-rich and S-rich MoS_2 in the absorption spectra could be attributed to the different electron doping effects. The AFM morphology and surface potential mapping for the monolayer Mo-rich and S-rich MoS_2 with a Au electrode on SiO_2/Si substrates are shown in Fig. S2.† The CVD-grown Mo-rich MoS_2 exhibited a work function of ∼96 meV, which is lower than that of the S-rich MoS_2.

A configuration similar to a back-gated FET was used for electrostatically controlled excitonic PL emission in CVD-grown monolayer MoS_2 on a SiO_2/Si substrate, as shown in Fig. 2(a). The PL spectra of our MoS_2 samples without electrostatic

doping in Fig. 2(b) exhibit clear peaks at 1.83–1.86 eV (A-excitonic emission) and an inconspicuous peak at near 2.0 eV (B-excitonic emission). This MoS_2 monolayer on a SiO_2/Si substrate showed PL bands that were red-shifted with respect to the peak positions of high-quality exfoliated monolayers, which is typical of the CVD-grown monolayer MoS_2 and caused by intrinsic strain and defects. The S-rich MoS_2 sample also presented a blue-shifted PL peak with a PL intensity that was 2.2-fold higher compared to the Mo-rich MoS_2 under laser excitation with a power intensity of $<10^3$ W cm^{-2}. The greater PL emission observed in the S-rich MoS_2 is consistent with the Raman spectra results. Fig. 2(c and d) presents the PL spectra at different V_g for the S-rich and Mo-rich MoS_2 samples with Au and P^+–Si as the electrodes. Both the S-rich and Mo-rich MoS_2 samples exhibited remarkably gate-dependent excitonic PL emission. Application of a negative V_g enhanced the A-excitonic PL intensity, while an applied positive V_g markedly reduced the A-excitonic PL. The PL peak positions of the S-rich MoS_2 remained almost constant at ∼1.855 eV for the main excitonic PL within a range of -40 V to $+40$ V of the applied V_g. However, in the Mo-rich MoS_2 samples, both the PL intensity and PL peak positions were noticeably changed. The main excitonic PL peak
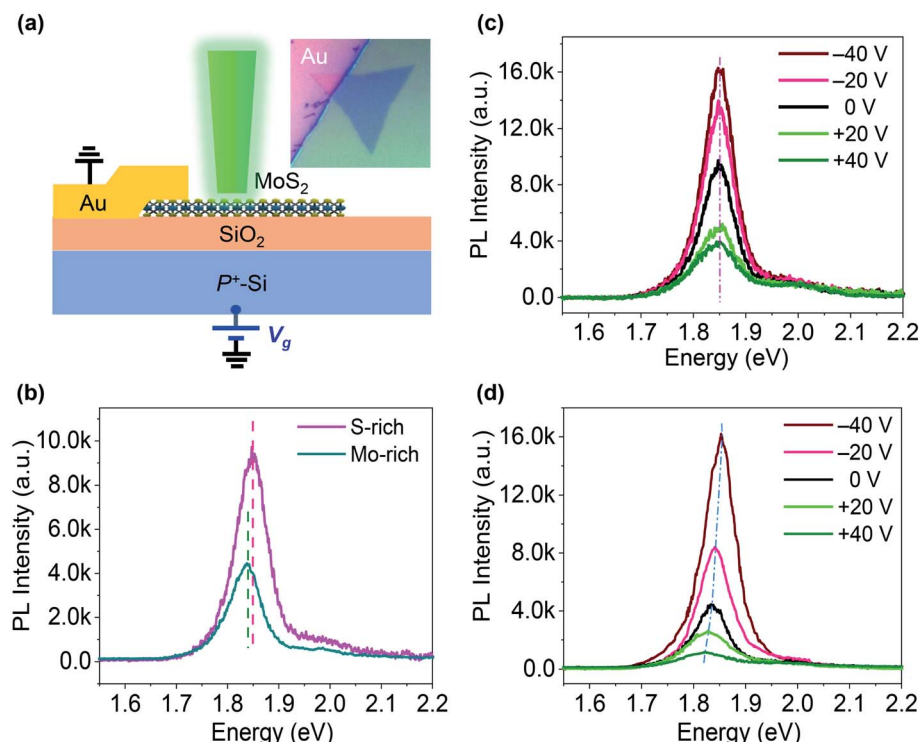
Fig. 2 (a) Schematic diagram of the experimental setup for the electrostatic doping of CVD-grown MoS_2; inset: optical image of the sample; (b) PL spectra of the monolayer MoS_2 samples without electrostatic doping; (c and d) PL spectra at various V_g for (c) S-rich MoS_2 and (d) Mo-rich MoS_2.

of the Mo-rich MoS_2 was located at 1.835 eV at $V_g = 0$ V, and then shifted to 1.823 eV at $V_g = +40$ V and 1.851 eV at $V_g = -40$ V, respectively.

To clarify the changes in A-excitonic and B-excitonic PL emission at different applied V_g, the PL spectra of MoS_2 were fitted with Lorentzian curves. The three peaks were denoted by the emission of neutral excitons (A^0), trions (A^-) and B excitons. The gate-dependent PL spectral fittings of the S-rich MoS_2 sample are shown in Fig. 3, with three PL peaks at 1.86 eV, 1.82 eV and 2.00 eV. A negative V_g could enhance the A-excitonic PL intensity (A^0 and A^-), but decrease the PL intensity from B excitons. When the V_g was adjusted to the positive range, the A-excitonic PL decreased, but B-excitonic PL increased and the peak became obvious. Quantitative analysis was conducted to assign the changes in PL intensity to the contribution of A^0, A^- or B. The normalized PL at various V_g suggested almost unshifted PL peaks and obvious changes in the B-excitonic PL intensity. The respective PL intensity and relative spectral weight distribution can be attributed to the free electron density in monolayer MoS_2, which can be changed by the applied V_g and gaseous environments. Fig. 3(f) shows the PL intensity ratio of A^0 and A^- ($I_{exciton}/I_{trion}$) of the S-rich MoS_2 at different V_g. The $I_{exciton}/I_{trion}$ ratio decreased monotonically from 2.08 to 0.86 as the V_g was adjusted from -40 V toward $+40$ V.

The electron density n_{el} in monolayer MoS_2 can be estimated from the PL intensity analysis of neutral exciton and trion emissions according to the mass action model based on the dynamic equilibrium between A excitons (A^0 and A^-) and free electrons, which can be expressed as:[15,39]

$$n_{el} = \frac{I_{A^-}}{I_{A^0}} \times \frac{\gamma_{A^0}}{\gamma_{A^-}} \times \left[\left(\frac{4 m_{A^0} m_e}{\pi \hbar^2 m_{A^-}} \right) k_B T \exp\left(-\frac{E_b}{k_B T} \right) \right] \quad (1)$$

Here, k_B is the Boltzmann constant, E_b is the trion binding energy ($\sim$20 meV),[21] m_0 is the mass of free electrons, and m_e (0.35 m_0), m_{A^0} (0.8 m_0), and m_{A^-} (1.15 m_0) are the effective masses of electrons, A^0 and A^-, respectively. I_{A^0} and I_{A^-} are the integrated PL intensities of A^0 and A^-, respectively, while γ_{A^0} and γ_{A^-} are the relative decay rates of A^0 and A^-, respectively. The value of $\gamma_{A^-}/\gamma_{A^0}$ is $\sim$0.15.[15] According to the PL intensity ratio $I_{exciton}/I_{trion}$, the electron density n_{el} at each V_g in the S-rich MoS_2 was calculated, as shown in Fig. 3(f). According to eqn (1), the estimated electron density in the S-rich MoS_2 was $\sim$1.47 $\times$ 10^{13} cm^{-2} at $V_g = 0$ V. At $V_g = -40$ V, and the calculated value of electron density in the S-rich MoS_2 sample was $\sim$1.20 $\times$ 10^{13} cm^{-2}, while at $V_g = +40$ V, the value was $\sim$2.89 $\times$ 10^{13} cm^{-2}.

The gate-dependent PL spectra of the Mo-rich MoS_2 sample were fitted with the Lorentzian function, with three peaks denoted by the emissions of A^0, A^-, and B excitons, corresponding to the energies of 1.852 eV, 1.812 eV and 1.962 eV, respectively. As shown in Fig. 4, the A-excitonic PL intensity decreased when V_g changed from -40 V to $+40$ V, but the B-excitonic PL increased and the peak became obvious. The quantitative analysis can assign the changes in PL intensity to the contributions of A^0, A^-, and B. The normalized PL at various V_g suggested the shifted A-excitonic PL peaks and obvious
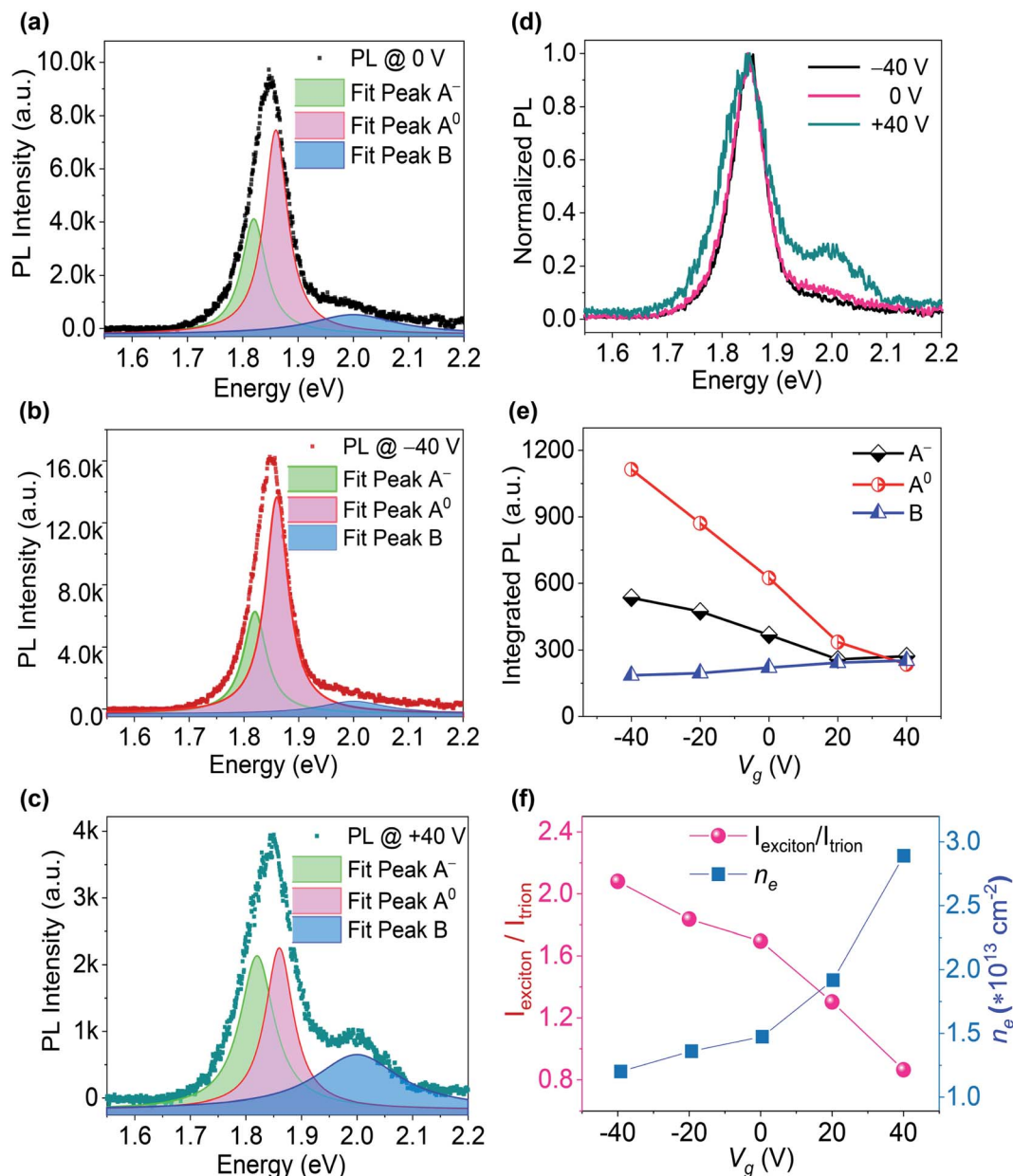
Fig. 3 Gate-dependent PL properties of the S-rich monolayer MoS_2 sample: (a–c) PL at $V_g = 0$ V, −40 V and +40 V, fitted by using the Lorentzian function; (d) normalized PL at $V_g = 0$ V, −40 V, and +40 V; (e) integrated PL intensities of A^0, A^-, and B; (f) ratio of the integrated PL intensities of A^0 and A^- *versus* V_g, and calculated electron density *versus* V_g.

changes in B-excitonic PL intensity. The PL emission of A^0 and A^- steadily decreased and the B-excitonic PL intensity increased monotonically when V_g was adjusted from −40 V to +40 V. As shown in Fig. 4(f), the $I_{exciton}/I_{trion}$ ratio of Mo-rich MoS_2 decreased monotonically from 1.69 to 0.18 as V_g was changed from −40 V toward +40 V. The calculated value of the electron density n_{el} in Mo-rich MoS_2 was ~3.36×10^{13} cm^{-2} at $V_g = 0$ V, ~1.48×10^{13} cm^{-2} at $V_g = -40$ V, and ~1.42×10^{14} cm^{-2} at $V_g = +40$ V. Moreover, the statistical value of the PL intensity ratio for both the S-rich and Mo-rich MoS_2 with error bars were obtained from more than 10 tests, as shown in Fig. S3.† At $V_g = -40$ V, the A-excitonic PL intensity ratio $I_{exciton}/I_{trion}$ of Mo-rich

MoS_2 was approximately 12-fold that of the ratio at $V_g = +40$ V. The PL intensity ratio of B and A excitons (I_B/I_A) was approximately 26 times higher at $V_g = +40$ V, compared to that at $V_g = -40$ V. Both the $I_{exciton}/I_{trion}$ and I_B/I_A ratios in Mo-rich MoS_2 were more sensitive to the applied V_g than that in S-rich MoS_2.

Generally, the as-prepared MoS_2 is *n*-doped due to the presence of unavoidable defects or unintentional doping of substrates. The excitonic PL in monolayer MoS_2 varies according to the changes in electron density and strain effects. By applying a negative V_g, holes are injected into MoS_2 and bind with excess electrons to form A^0 excitons, resulting in pronounced trion-exciton conversion and enhanced PL
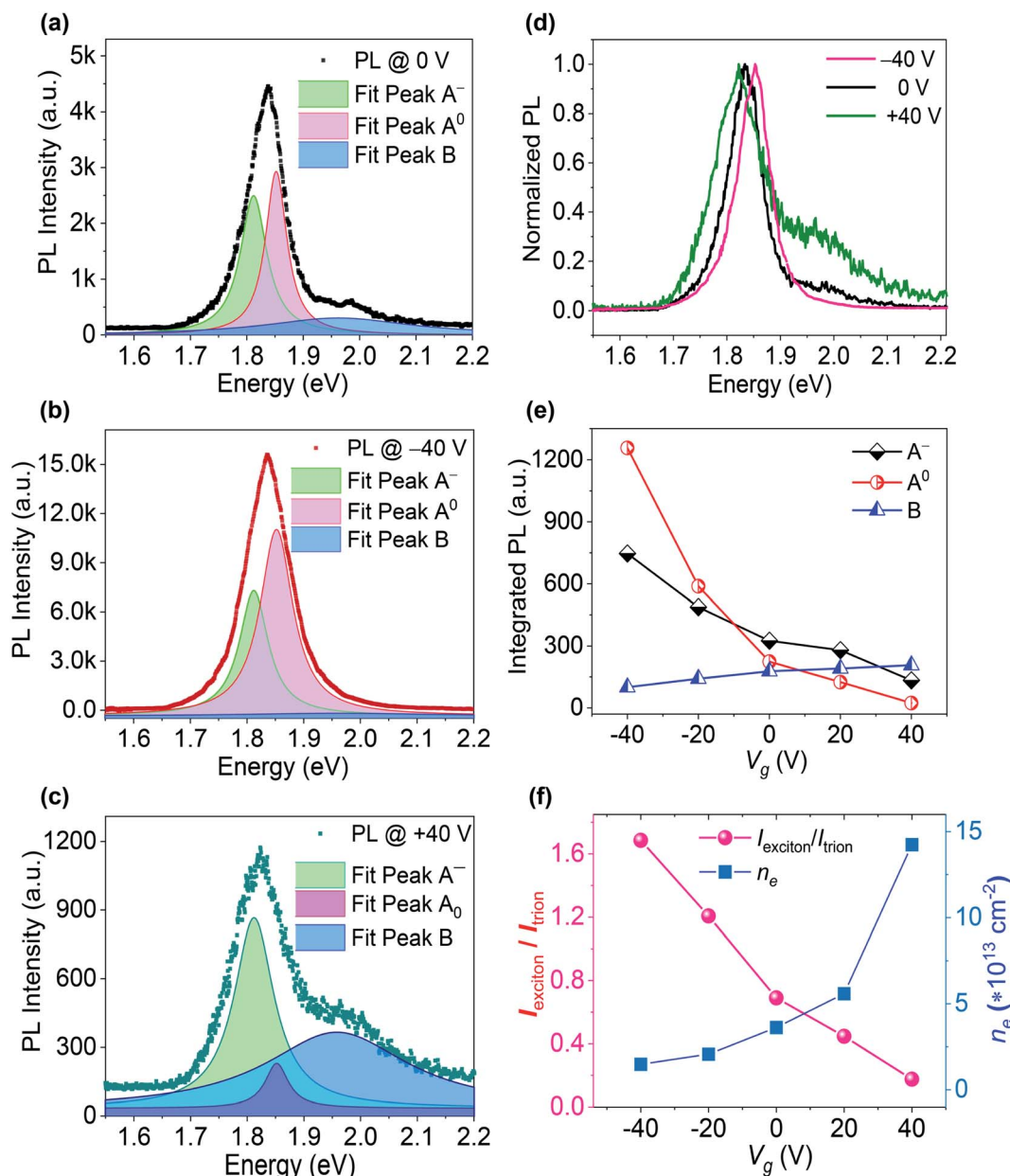
Fig. 4 Gate-dependent PL properties of the Mo-rich monolayer MoS$_2$ sample: (a–c) PL at $V_g = 0$ V, −40 V and +40 V, fitted with the Lorentzian function; (d) normalized PL at $V_g = 0$ V, −40 V and +40 V; (e) integrated PL intensities of A^0, A$^-$, and B; (f) ratio of the integrated PL intensities of A^0 and A$^-$ versus V_g, and calculated electron density versus V_g.

intensity in the A-exciton band. The enhanced A^0 and A$^-$ emission can be attributed to the suppression of non-radiative recombination of A^0 and A$^-$ at the defect sites, as well as the proposed transition from B to A exciton recombination. Meanwhile, at a positive V_g, n-type doping with injected electrons facilitates the increased formation of A$^-$, leading to a decrease in both the A^0 exciton density and total PL intensity. The probability of forming excitons and trions is expected to rapidly decrease at a high electron density in MoS$_2$ due to the nonradiative recombination via the Auger process, which leads to a low PL intensity from A excitons. The excitonic PL intensity from A$^-$ decreased monotonically even when the

applied V_g changed from negative to positive in our experiment. The trion PL in our study seems more sensitive to V_g than that in the former reported results, where the trion PL is nearly gate independent or exhibits weak gate bias dependence.

The applied gate voltage can be converted to the charge carrier doping density ($\Delta n_{injected} = CV_g/e$), where $C = \varepsilon_0\varepsilon_r/d$, $\varepsilon_0 = 8.85 \times 10^{-12}$ F m^{-1}, $\varepsilon_r = 3.9$, and $d = 280$ nm. The injected hole density was ∼3 × 10^{12} cm^{-2} at $V_g = -40$ V, while the injected electron density was ∼3 × 10^{12} cm^{-2} at $V_g = +40$ V. It should be noted that in the S-rich MoS$_2$ sample, the calculated $\Delta n_{injected}$ was almost equivalent to the inferred electron density change

(Δn_{el}) from $I_{exciton}/I_{trion}$ at $V_g = -40$ V but much smaller than that at $V_g = +40$ V. In the Mo-rich MoS_2 sample, the calculated $\Delta n_{injected}$ was much smaller than the inferred Δn_{el} at a both negative and positive V_g. Furthermore, the inferred Δn_{el} from $I_{exciton}/I_{trion}$ at $V_g = -40$ V was smaller than that at $V_g = +40$ V in both the S-rich and Mo-rich MoS_2 samples. The different electron density changes Δn_{el} in S-rich and Mo-rich MoS_2 could be attributed to the different gas adsorption situations of MoS_2 at a positive and negative V_g.

Sulfur vacancies in monolayer MoS_2 have the lowest formation energy and can act as active centers for trapping molecules and chemical reactions. Generally, the physically and chemically adsorbed ambient gas molecules on the MoS_2 surface can reduce the electron density and enhance the PL intensity with a blue shift.[40–42] Due to the interactions of O_2 and H_2O molecules with S vacancies, charge transfer from defective MoS_2 to O_2/H_2O leads to a decrease in the relative trion intensity.[43] Considering the basic electrostatics theory, the SiO_2–MoS_2 interface either attracts electrons or repels electrons to or from O_2, depending on the polarity.[44] Charge transfer between the adsorbed molecule and MoS_2 can even be significantly modulated by a perpendicular electric field.[45] Therefore, the physically adsorbed molecules on monolayer MoS_2 can act as either charge acceptors or donors, depending on the situation. The applied V_g can consistently modify the charge transfer between the adsorbed molecules and monolayer MoS_2. Since the electron density is further reduced in MoS_2 when a negative V_g was applied with hole-doping, the charge transfer from MoS_2 to the adsorbed molecules could be suppressed. Meanwhile, the positive V_g induced by electron-doping resulted in an increased density of electrons in MoS_2, which may affect the charge transfer between MoS_2 and O_2/H_2O molecules, and lead to an adsorption situation different from that of MoS_2 at a negative V_g. Since the position of the Fermi level can significantly influence the adsorption and desorption processes of oxygen molecules on the surface,[13,40] we suppose that the external
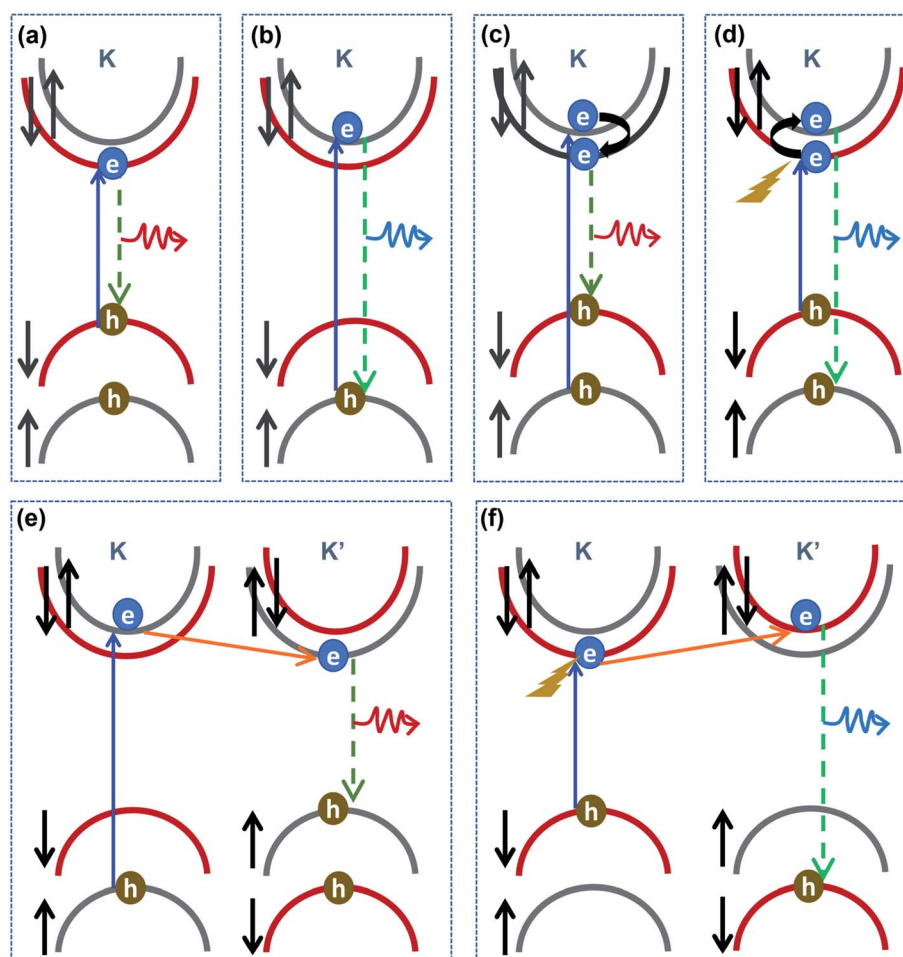

Fig. 5 (a and b) Traditional excitonic radiative recombination at the K valley for A and B excitons, respectively; (c–f) intravalley and intervalley transition processes in monolayer MoS_2: (c) at the K valley, a spin-up electron in the valence band (VB) is excited to the spin-up conduction band (CB), then it scatters to the spin-down CB at the K valley before A-excitonic recombination occurs; (d) at the K valley, a spin-down VB electron is excited to the spin-down CB, then phonon-assisted spin–flip intravalley scattering occurs before B-excitonic recombination; (e) at the K valley, a spin-up VB electron is excited to the spin-up CB, then intervalley scattering occurs before A-excitonic recombination at the K' valley; (f) at the K valley, a spin-down VB electron is excited to the spin-down CB, then phonon-assisted intervalley scattering occurs before B-excitonic recombination at the K' valley.

absorption of O_2/H_2O molecules from the ambient environment partly depends on the different electrostatic dopings in monolayer MoS_2. The S-rich MoS_2 sample doped with PEDOT : PSS was used to confirm the effects of gas adsorption and surface defects. After doping with PEDOT : PSS, the sulfur vacancies can be healed spontaneously by the sulfur ad atom clusters through PSS-induced hydrogenation.[17] The PEDOT : PSS layer even insulated MoS_2 from the H_2O/O_2 in air, leading to suppressed charge transfer between the MoS_2 surface and the gas molecules. Fig. S4† shows the PL spectra and integrated PL intensity of the doped MoS_2 sample at different V_g. The PL intensity from A^- in the doped MoS_2 showed a weak dependence on V_g, similar to the results in previously reported studies. Thereby, the monotonic change in the intensity of A-excitonic PL as the V_g increased from -40 V to $+40$ V can be attributed to variations in charge density, which were simultaneously affected by electrostatic doping and gas adsorption in both S-rich and Mo-rich MoS_2.

Another key issue is the PL emission of B excitons, which changes with electrostatic doping in MoS_2. Generally, A and B excitons are quickly formed at K and K' valleys under photo-excitation with circular polarization. After the excitons are generated, besides the direct excitonic radiative recombination at the K and K' valleys, A and B excitons can also undergo intravalley and intervalley scattering before recombination, as shown in Fig. 5. The B excitons can serve as a population supplier to the energetically lower A excitons.[46] As shown in Fig. 5(c) and (e), the rapid relaxation from B to A excitons reduces the available B-excitonic PL emission while simultaneously increasing the A-excitonic PL. Meanwhile, as shown in Fig. 5(d) and (f), the photoexcited electron with a spin-down state for the A exciton at the K valley can exhibit an intravalley spin reversal to occupy the electron spin-up state for the B exciton at the K valley, or exhibit intervalley scatter to the electron spin-down state for the B exciton at the K' valley. The intravalley transition with electron spin reversal can be mediated by flexural phonons *via* the Elliott–Yafet spin-flip mechanism due to intrinsic electron–phonon scattering.[47–49] These intravalley and intervalley transitions from A to B excitons can also be understood as a phonon-assisted process. Auger recombination leads to the annihilation of electrons in the conduction band and holes in valence sub-band A, while creating phonons coupled with electrons. Then, electron–phonon coupling contributes to the new formation of B excitons.

Since the effective exciton lifetime of both A and B excitons are sensitive to the density of defects due to the induced non-radiative recombination pathways, the transition between A and B excitons would be affected by the defect density in MoS_2. High electron density in MoS_2 can result in significantly different non-radiative recombinations, resulting in a greater B exciton population available due to the phonon-assisted process. Furthermore, typical electrostatic gating and the dielectric environment of 2D materials can break the σ_h symmetry and induce electron–phonon coupling to the flexural phonon modes, which manifest in a linear dependence on the electron density *via* the gate voltages.[50]

Consequently, the increased electron–phonon coupling would enhance electron spin reversal when more electrons are injected into MoS_2, leading to an obvious enhancement in the B exciton population with the phonon-assisted process. Thereby, we explain the observed increase of B excitonic emission with increasing electron density by considering the enhanced intravalley A-to-B exciton transition as a result of the phonon-assisted process. The B-excitonic PL intensity increased due to the transition from A to B excitons when more electrons were injected by a negative V_g, while the reduction of B-excitonic PL emission could be attributed to the B to A exciton relaxation effect in a hole-doping situation under the condition of a negative V_g.

Conclusions

In summary, excitonic PL from both A excitons and B excitons in monolayer CVD-grown MoS_2 was investigated at room temperature. Electrostatic doping through V_g variation was shown to be an effective control method for the A-excitonic and B-excitonic PL in monolayer MoS_2 with different defect densities. Electrostatic doping led to a change in the B-excitonic PL intensity that occurred in the opposite direction to changes in A-excitonic PL. The applied positive V_g promoted electron injection and obviously enhanced the PL intensity from B excitons, while the A-excitonic PL was suppressed in both S-rich and Mo-rich monolayer MoS_2. Our results demonstrate not only the ability to control the conversion between A^0 and A^- through the combination of gas adsorption and electrostatic doping, but also the presence of transitions between A excitons and B excitons. The B excitons would relax to A excitons when a negative V_g was applied, leading to reduced B exciton population and increased A-excitonic PL. When the applied V_g became positive with electron doping, the population of B excitons was promoted due to the intravalley and intervalley transition from A excitons, which can be mediated by flexural phonons in the realm of the Elliott–Yafet spin–flip mechanism through electron–phonon coupling. In Mo-rich monolayer MoS_2, a 12-fold increase in the A-excitonic PL intensity ratio $I_{exciton}/I_{trion}$ was observed at a V_g of -40 V and an approximately 26-fold increase in I_B/I_A occurred at the applied V_g of $+40$ V. This electrostatic doping method could offer an important method for excitonic PL modulation. The efficient tunability of B-excitonic PL emission may provide potential applications in exciton physics and valleytronic devices involving the B excitons.

Conflicts of interest

There are no conflicts to declare.

Acknowledgements

Notes and references

1 M. Amani, D.-H. Lien, D. Kiriya, J. X. A. Azcatl, J. Noh, S. R. Madhvapathy, R. Addou, K. C. Santosh, M. Dubey, K. Cho, R. M. Wallace, S.-C. Lee, J.-H. He, J. W. Ager III, X. Zhang, E. Yablonovitch and A. Javey, *Science*, 2015, **350**, 1065–1068.

2 F. Liao, J. Yu, Z. Gu, Z. Yang, T. Hasan, S. Linghu, J. Peng, W. Fang, S. Zhuang, M. Gu and F. Gu, *Sci. Adv.*, 2019, **5**, eaax7398.

3 N. Li, Q. Wang, C. Shen, Z. Wei, H. Yu, J. Zhao, X. Lu, G. Wang, C. He, L. Xie, J. Zhu, L. Du, R. Yang, D. Shi and G. Zhang, *Nat. Electron.*, 2020, **3**, 711–717.

4 D. Mouloua, A. Kotbi, G. Deokar, K. Kaja, M. E. Marssi, M. A. E. Khakani and M. Jouiad, *Materials*, 2021, **14**, 3283.

5 Y. C. Liu and F. X. Gu, *Nanoscale Adv.*, 2021, **3**, 2117–2138.

6 H. Wang, C. Li, P. Fang, Z. Zhang and J. Z. Zhang, *Chem. Soc. Rev.*, 2018, **47**, 6101–6127.

7 D. B. Sulas-Kern, E. M. Miller and J. L. Blackburn, *Energy Environ. Sci.*, 2020, **13**, 2684–2740.

8 T. Mueller and E. Malic, *npj 2D Mater. Appl.*, 2018, **2**, 29.

9 X. Dou, K. Ding, D. Jiang, X. Fan and B. Sun, *ACS Nano*, 2016, **10**, 1619–1624.

10 K. M. McCrearya, A. T. Hanbicki, V. S. Sa and B. T. Jonker, *APL Mater.*, 2018, **6**, 111106.

11 Y. Cai, H. Zhou, G. Zhang and Y.-W. Zhang, *Chem. Mater.*, 2016, **28**, 8611–8621.

12 D.-H. Lien, S. Z. Uddin, M. Yeh, M. Amani, H. Kim, J. W. Ager, E. Yablonovitch and A. Javey, *Science*, 2019, **364**, 468–471.

13 P. Klement, C. Steinke, S. Chatterjee, T. O. Wehling and M. Eickhoff, *2D Mater.*, 2018, **5**, 045025.

14 P. K. Gogoi, Zh. Hu, Q. Wang, A. Carvalho, D. Schmidt, X. Yin, Y.-H. Chang, L.-J. Li, C. H. Sow, A. H. Castro Neto, M. B. H. Breese, A. Rusydi and A. T. S. Wee, *Phys. Rev. Lett.*, 2017, **119**, 077402.

15 S. Mouri, Y. Miyauchi and K. Matsuda, *Nano Lett.*, 2013, **13**, 5944–5948.

16 M. Amani, R. A. Burke, X. Ji, P. Zhao, D.-H. Lien, P. Taheri, G. H. Ahn, D. Kirya, J. W. Ager III, E. Yablonovitch, J. Kong, M. Dubey and A. Javey, *ACS Nano*, 2016, **10**, 6535–6541.

17 X. Zhang, Q. Liao, S. Liu, Z. Kang, Z. Zhang, J. Du, F. Li, S. Zhang, J. Xiao, B. Liu, Y. Ou, X. Liu, L. Gu and Y. Zhang, *Nat. Commun.*, 2017, **8**, 15881.

18 J. S. Ross, S. Wu, H. Yu, N. J. Ghimire, A. M. Jones, G. Aivazian, J. Yan, D. G. Mandrus, D. Xiao, W. Yao and X. Xu, *Nat. Commun.*, 2013, **4**, 1474.

19 L. A. Jauregui, A. Y. Joe, K. Pistunova, D. S. Wild, A. A. High, Y. Zhou, G. Scuri, K. De Greve, A. Sushko, C.-H. Yu, T. Taniguchi, K. Watanabe, D. J. Needleman, M. D. Lukin, H. Park and P. Kim, *Science*, 2019, **366**, 870–875.

20 J. Xiao, M. Zhao, Y. Wang and X. Zhang, *Nanophotonics*, 2017, **6**(6), 1309–1328.

21 K. F. Mak, K. He, C. Lee, G. H. Lee, J. Hone, T. F. Heinz and J. Shan, *Nat. Mater.*, 2013, **12**, 207–211.

22 M. Zhou, W. Wang, J. Lu and Z. Ni, *Nano Res.*, 2021, **14**, 29–39.

23 A. Steinhoff, J.-H. Kim, F. Jahnke, M. Rösner, D.-S. Kim, C. Lee, G. H. Han, M. S. Jeong, T. O. Wehling and C. Gies, *Nano Lett.*, 2015, **15**, 6841–6847.

24 K. Wu, Z. Li, J. Tang, X. Lv, H. Wang, R. Luo, P. Liu, L. Qian, S. Zhang and S. Yuan, *Nano Res.*, 2018, **11**, 4123–4132.

25 G. M. Akselrod, T. Ming, C. Argyropoulos, T. B. Hoang, Y. Lin, X. Ling, D. R. Smith, J. Kong and M. H. Mikkelsen, *Nano Lett.*, 2015, **15**, 3578–3584.

26 J. Huang, G. M. Akselrod, T. Ming, J. Kong and M. H. Mikkelsen, *ACS Photonics*, 2018, **5**, 552–558.

27 K. M. McCrearya, A. T. Hanbicki, S. V. Sivaramb and B. T. Jonker, *APL Mater.*, 2018, **6**, 111106.

28 A. S. Sarkar, I. Konidakis, I. Demeridou, E. Serpetzoglou, G. Kioseoglou and E. Stratakis, *Sci. Rep.*, 2020, **10**, 15697.

29 S. Wang, Y. Rong, Y. Fan, M. Pacios, H. Bhaskaran, K. He and J. H. Warner, *Chem. Mater.*, 2014, **26**, 6371–6379.

30 H. Liu, Y. Zhu, Q. Meng, X. Lu, S. Kong, Z. Huang, P. Jiang and X. Bao, *Nano Res.*, 2017, **10**, 643–651.

31 I. S. Kim, V. K. Sangwan, D. Jariwala, J. D. Wood, S. Park, K.-S. Chen, F. Shi, F. Ruiz-Zepeda, A. Ponce, M. Jose-Yacaman, V. P. Dravid, T. J. Marks, M. C. Hersam and L. J. Lauhon, *ACS Nano*, 2014, **8**, 10551–10558.

32 D. Zhou, H. Shu, C. Hu, L. Jiang, P. Liang and X. Chen, *Cryst. Growth Des.*, 2018, **18**, 1012–1019.

33 Y. Zhan, Z. Liu, S. Najmaei, P. M. Ajayan and J. Lou, *Small*, 2012, **8**, 966–971.

34 A. Tarasov, S. Zhang, M. Y. Tsai, P. M. Campbell, S. Graham, S. Barlow, S. R. Marder and E. M. Vogel, *Adv. Mater.*, 2015, **27**, 1175–1181.

35 M. W. Iqbal, K. Shahzad, R. Akbar and G. Hussain, *Microelectron. Eng.*, 2020, **219**, 111152.

36 W. H. Chae, J. D. Cain, E. D. Hanson, A. A. Murthy and V. P. Dravid, *Appl. Phys. Lett.*, 2017, **111**, 143106.

37 S. E. Panasci, E. Schilirò, G. Greco, M. Cannas, F. M Gelardi, S. Agnello, F. Roccaforte and F. Giannazzo, *ACS Appl. Mater. Interfaces*, 2021, **13**, 31248–31259.

38 G. Ciampalini, F. Fabbri, G. Menichetti, L. Buoni, S. Pace, V. Mišeikis, A. Pitanti, D. Pisignano, C. Coletti, A. Tredicucci and S. Roddaro, *ACS Nano*, 2022, **16**, 1291–1300.

39 Y. Li, Z. Qi, M. Liu, Y. Wang, X. Cheng, G. Zhang and L. Sheng, *Nanoscale*, 2014, **6**, 15248–15254.

40 H. Nan, Z. Wang, W. Wang, Z. Liang, Y. Lu, Q. Chen, D. He, P. Tan, F. Miao, X. Wang, J. Wang and Z. Ni, *ACS Nano*, 2014, **8**, 5738–5745.

41 J. H. Kim, J. Lee, J. H. Kim, C. C. Hwang, C. Lee and J. Y. Park, *Appl. Phys. Lett.*, 2015, **106**, 251606.

42 C. Hou, J. Deng, J. Guan, Q. Yang, Z. Yu, Y. Lu, Z. Xu, Z. Yao and J. Zheng, *Phys. Chem. Chem. Phys.*, 2021, **23**, 24579–24588.

43 B. Birmingham, J. Yuan, M. Filez, D. Fu, J. Hu, J. Lou, M. O. Scully, B. M. Weckhuysen and Z. Zhang, *ACS Appl. Nano Mater.*, 2018, **1**, 6226–6235.

44 P. Klement, C. Steinke, S. Chatterjee, T. O Wehling and M. Eickhoff, *2D Mater.*, 2018, **5**, 045025.

45 Q. Yue, Z. Shao, S. Chang and J. Li, *Nanoscale Res. Lett.*, 2013, **8**, 425.

46 S. Cha, J. H. Sung, S. Sim, J. Park, H. Heo, M.-H. Jo and H. Choi, *Nat. Commun.*, 2016, **7**, 10768.

47 Y. Song and H. Dery, *Phys. Rev. Lett.*, 2013, **111**, 026601.

48 E. J. Sie, A. J. Frenzel, Y.-H. Lee, J. Kong and N. Gedik, *Phys. Rev. B*, 2015, **92**, 125417.

49 C. Mai, A. Barrette, Y. Yu, Y. G. Semenov, K. W. Kim, L. Cao and K. Gundogdu, *Nano Lett.*, 2014, **14**, 202–206.

50 T. Gunst, K. Kaasbjerg and M. Brandbyge, *Phys. Rev. Lett.*, 2017, **118**, 046601.